Wideband microwave magnetometry using a nitrogen-vacancy center in diamond

Rui Li,[1,2,3] Cheng-Jie Wang,[1,3,4] Zhi Cheng,[1,2,3] Pengfei Wang,[1,2,3,*] Ya Wang,[1,2,3] Changkui Duan,[1,3,4] Hangyu Liu,[1,2,3] Fazhan Shi,[1,2,3] and Jiangfeng Du[1,2,3,†]

[1]*CAS Key Laboratory of Microscale Magnetic Resonance and Department of Modern Physics, University of Science and Technology of China (USTC), Hefei 230026, China*

[2]*Hefei National Laboratory for Physical Sciences at the Microscale, USTC, Hefei 230026, China*

[3]*Synergetic Innovation Center of Quantum Information and Quantum Physics, USTC, Hefei 230026, China*

[4]*Department of Physics, USTC, Hefei 230026, China*

(Received 7 November 2018; published 24 June 2019)

Microwave magnetometry is essential to a variety of modern electronic techniques, most notably integrated circuits. The nitrogen-vacancy center in diamond has shown the ability of nanoscale resolution for the microwave magnetic field measurement and imaging. However, the characterization of the wideband magnetic field remains a challenge. Here we experimentally demonstrated a wideband microwave magnetometry with an off-resonance protocol based on the Bloch-Siegert shift effect. The off-resonance microwave magnetic field shifts the energy level of the nitrogen-vacancy center. It results in a phase accumulation during the evolution of the superposition state of the quantum sensor. According to this effect, by optimizing the evolution time, we experimentally verified the bandwidth widening of an order of magnitude compared with the Rabi oscillation, i.e., on-resonance method with an acceptable decrease of the sensitivity. In addition, we extracted the microwave frequency with a two-qubit system, which consists of a nitrogen-vacancy center and a nearby ^{13}C nucleus. This approach enables the building of a wideband and potentially nanoscale microwave magnetometry to allow various potential applications, such as electronic circuits development.

DOI: 10.1103/PhysRevA.99.062328

I. INTRODUCTION

Nanoscale and wideband magnetic field magnetometry provides a key technique to develop modern electronic circuits, such as microchips. As the linewidth of current devices has been pushed forward to several nanometers [1], the crosstalk [2] cannot be neglected, which makes near-field characterization inevitable [3]. Furthermore, electronic circuits rely on the ultrawideband (UWB) technique to transmit information with a pulsed electromagnetic wave [4] in the bandwidth of several gigahertz. The characterization of nanoscale and wideband magnetic fields thus provides a powerful diagnosis tool for electronic circuits, which, however, remains a major challenge.

The classical sensors, such as loop antennas [5], transduce the microwave (MW) to electrical signals caused by the electromagnetic-field-induced charge motion. For such sensors, careful design and calibration are necessary because the frequency response is highly related to the geometry and developing technology [6]. Another limitation of the classical probe is that the spatial resolution is inadequate for the near-field electromagnetic test [3,7,8].

Benefiting from the quantum evolution under quantum mechanics, quantum sensors based on spins do not need complicated calibrations under various frequencies [9,10]. Previously, single trapped ions [11], ultracold atoms [12,13], and superconducting quantum interference devices [14] were used to probe the MW magnetic field at various frequencies in the submicrometer, micrometer, and submillimeter scale resolutions, respectively. However, they work only in ultrahigh vacuum or at low temperature, which limits their applications.

The recently developed solid-state quantum sensor named the nitrogen-vacancy (NV) center in diamond works under ambient conditions and has shown the ability of nanometer-scale magnetic field sensing and imaging [15–17]. Recent studies investigated the sensing of MW magnetic fields by Rabi oscillation under resonant MW driving [18–21] and pulsed Mollow absorption spectroscopy under near-resonance MW driving [22] with a careful tuning of the magnetic field and prior knowledge of the MW frequency. However, measuring fields over a large frequency bandwidth, which is essential for MW magnetometry, has not been achieved.

High bandwidth becomes more and more important in today's device design and fabrications, such as on-chip and in-package antennas, amplifiers, and other related devices, and chips for wideband communications (for example, 3G, 4G, or 5G [23]). Even for the CPU, the technique called Turbo Boost (Intel) or Turbo Core (AMD) dynamically tune the working frequency in several hundreds of MHz. Furthermore, making the sensor work at a certain frequency usually needs a bias static magnetic field (for NV center) which may influence the performance of the electronic device. Last but not least, in the study of multiferroic material which has many frequencies, the large bandwidth will speed up the measurement. And the magnetic field to make the sensor work at a certain frequency will alter the multiferroic material frequency.

*wpf@ustc.edu.cn
†djf@ustc.edu.cn

Here, we propose and demonstrate a wideband MW quantum sensing protocol based on the Bloch-Siegert shift effect (BSE) [24,25] with a dynamical decoupling sequence [26] on a single NV center. We first investigate the BSE under various off-resonance MW frequencies. Then we study the sensitivity of the MW magnetic field measurement and demonstrate the sensing of a MW magnetic field detuned up to 4 GHz away from the resonance frequency. Finally, we demonstrate the extraction of the MW frequency by utilizing a two-qubit system, formed by an NV center and a nearby ^{13}C nuclear spin.

II. PRINCIPLE OF BSE FOR AN NV CENTER

The BSE of the NV center is a second-order effect caused by an off-resonance MW (OMW) magnetic field. The Hamiltonian of the NV center electron spin is written as

$$H = DS_z^2 + \gamma B_z S_z + \gamma B_{\mathrm{OMW}} \cos(f\tau) S_x, \tag{1}$$

where $D = 2.87$ GHz is the zero-field splitting and γ is the gyromagnetic ratio of the electronic spin. A static magnetic field $B_z = 50$ mT along the NV axis is applied to remove the degeneracy of the $|-1\rangle, |+1\rangle$ states and polarizes the nearby ^{14}N nuclear spin so that the hyperfine interaction between the NV center and the ^{14}N nuclear spin can be neglected [27]. B_{OMW} is the amplitude of the off-resonance MW magnetic field at the frequency f. τ is the duration of the MW applied. S_x and S_z are the Pauli matrices. The off-resonance MW term causes a small energy shift (details in Appendix A, B) in the rotation frame [Fig. 1(b)], namely, the BSE. The BSE corresponds to an effective magnetic field:

$$B_{\mathrm{eff}} = \tfrac{1}{8}\gamma B_{\mathrm{OMW}}^2 Q, \tag{2}$$

$$Q = \frac{1}{f_+ - f} + \frac{2}{f_- + f} + \frac{2}{f_- - f} + \frac{1}{f_+ + f}. \tag{3}$$

To measure the magnitude of the off-resonance MW, we used the quantum interference between the $|0\rangle$ and $|-1\rangle$ states. The BSE accumulates relative phase φ between $|0\rangle$ and $|-1\rangle$ states and the accumulated phase is written as

$$\varphi = \tfrac{1}{8}(\gamma B_{\mathrm{OMW}})^2 Q\tau. \tag{4}$$

In the case that the off-resonance frequency f is close to the transition frequency f_- between the $|0\rangle$ and $|-1\rangle$ states, $Q \approx 2/\Delta$ where $\Delta = f - f_-$ is the detuning from the resonance frequency. In the readout section, the quantum phase φ is transformed to the population of the $|0\rangle$ state by a $\pi/2$ pulse and measured by fluorescence intensity [28]. The population signal is normalized to

$$S = \tfrac{1}{2}[1 + \cos(\omega\tau)], \tag{5}$$

$$\omega = \frac{1}{4\Delta}\gamma^2 B_{\mathrm{OMW}}^2, \tag{6}$$

which indicates the BSE causes an oscillation between two energy levels of an NV center, noted as Bloch-Siegert (BS) oscillation.

Figure 2(a) shows an oscillation when the off-resonance MW is on and the oscillation disappears with the off-resonance MW off. To confirm that the oscillation comes

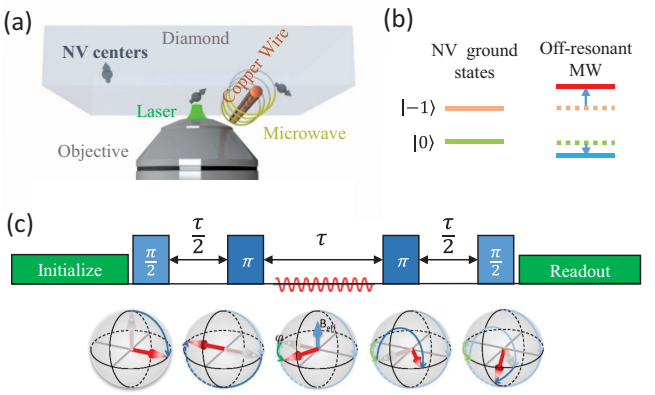

FIG. 1. Experiment setup and schematic diagram of BSE. (a) Experiment setup. A 532-nm green laser is focused on the NV center in diamond for polarization and readout. The copper wire delivers the MW magnetic field to manipulate the quantum spin as well as the off-resonance MW field for sensing. (b) Energy levels of the NV center of the $|0\rangle$ and $|-1\rangle$ subspace. The off-resonance MW causes a small energy shift. (c) Dynamical decoupling sequence to measure the BSE and the schematic view of the spin evolution. The quantum state is demonstrated on a Bloch sphere in the rotating frame corresponding to the NV's resonant frequency. The laser initializes the NV center to the $|0\rangle$ state and a $\pi/2$ pulse creates a superposition state. Then the NV center evolves during the first $\tau/2$ and after a π pulse, it accumulates a phase φ related to the B_{eff} during the evolution time τ. Another free induction evolves $\tau/2$ after a second π pulse. Finally, a $\pi/2$ pulse transforms the phase of the NV center to the population which is read out by the fluorescence intensity.

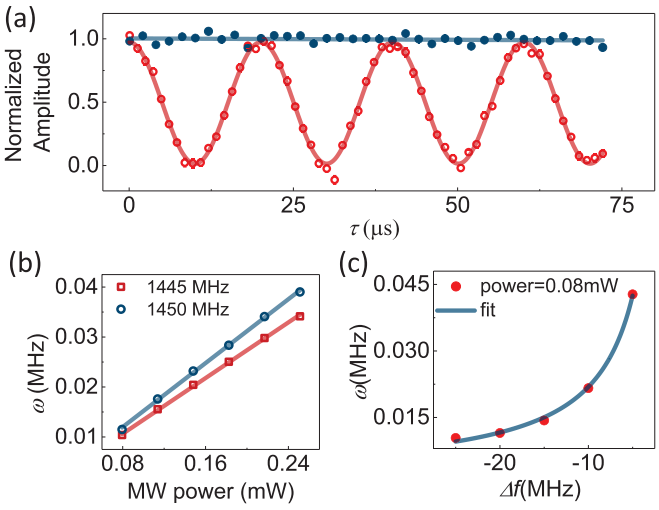

FIG. 2. Experimental observation of BSE. (a) The normalized signal versus evolution time with off-resonance MW on (red circles) and off (blue dots) with frequency at 1455 MHz. The red line shows a cosine fitting. The BS oscillation under the off-resonance MW corresponds to the BSE. (b) The frequency of BS oscillation versus MW power under two different off-resonance frequencies. As the output power of the MW source is proportional to B_{OMW}^2, the oscillation frequency is proportional to the MW source power. (c) The BS oscillation frequency ω against the detuning frequency of the applied MW in the range from -25 to -5 MHz and a fitting curve using $1/\Delta$.

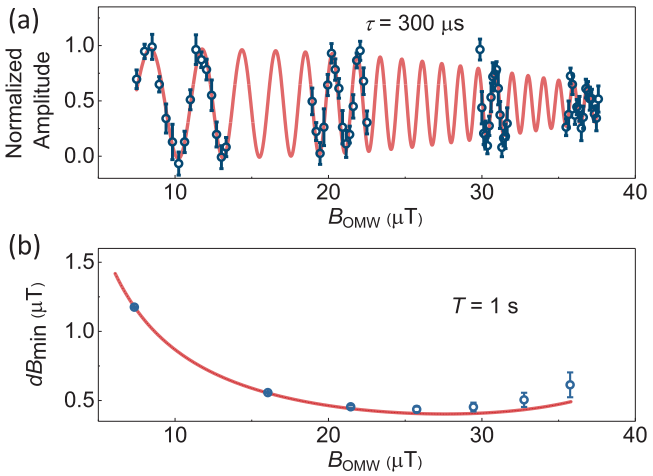

FIG. 3. Sensitivity of the magnetometer. (a) The signal of BS oscillation (recorded at $\tau = 300\ \mu$s) was measured while increasing the magnitude of the MW at a detuning frequency of -4 MHz. (b) The sensitivities are calculated against the magnitude B_{OMW}. The line is the simulation result. The error bars of the experimental data are calculated from the standard error of the fitting errors of (a).

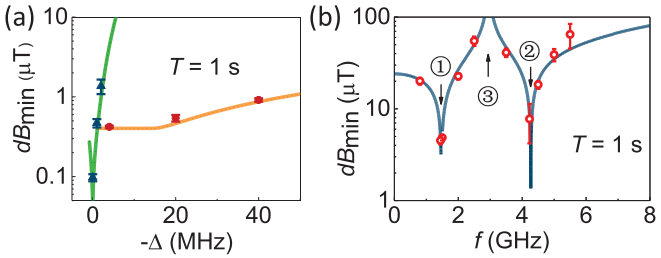

FIG. 4. Bandwidth measurement. (a) With B_{OMW} magnitude limited in no more than 100 μT, the maximal sensitivity is measured and simulated both in Rabi and BSE methods in 1 s. The orange and green lines are the simulation of the BSE and Rabi methods, respectively. The data points in red and blue are measured in BSE and Rabi experiments, separately. (b) The sensitivity of the magnetometer at different frequencies of the MW, calculated in the first period of the oscillation signal, is measured in 1 s ($T = 1$ s) (red dots). The blue line is the simulation curve. Numbers 1 and 2 correspond to the two resonance frequencies of the NV center while 3 comes from the singularity of Q.

from the BSE, we did the following experiments. First, the linear relationship shown by Fig. 2(b) indicates that the oscillation frequency ω is proportional to the power of the MW generator, i.e., B^2_{OMW}. Second, the inverse relationship between ω and the detuning frequency Δ is shown in Fig. 2(c). Those two relationships are correspond to Eq. (6). Then the oscillation comes from the BSE is confirmed and the B_{OMW} magnitude can be figured out from the input power of the off-resonance MW generator according to the BSE with the detuning frequency known.

III. SENSITIVITY OF BSE METHOD

To study the sensitivity of wideband MW magnetometry, we set the frequency as known information first, for example, detuning at $\Delta = -4$ MHz. As shown in Fig. 3(a), with the phase accumulated time τ optimized [15] to reach the best sensitivity and fixed, the oscillation comes as a sine wave with B^2_{OMW}. The decay of the envelope of the BS oscillation in Fig. 3(a) can be attributed to the natural broadening of the energy level of the NV center (details in Appendix D). The minimal distinguishable magnetic field δB_{min} is calculated by the standard deviation σ_S^N after N measurements divided by the absolute maximal slope dS_B of the normalized signal [15]. In the several initial periods where the decay can be neglected, $dS_B = \frac{1}{8}\gamma^2 B_{\mathrm{OMW}} Q$ is a linear function of B_{OMW}. Then the sensitivity η is given as

$$\eta = \delta B_{\mathrm{min}}\sqrt{T} = \frac{16\sigma_S}{\gamma^2 B_{\mathrm{OMW}} Q\sqrt{\tau}}, \tag{7}$$

where σ_S is the uncertainty of one measurement and T is the total measurement time (details in Appendix E).

Increasing B_{OMW} improves the sensitivity according to Eq. (7). However, when B_{OMW} becomes so large that the decay cannot be omitted, the sensitivity decreases. Figure 3(b) shows the minimal distinguishable magnetic field versus the MW amplitude B_{OMW} during 1 s measuring time, and finally gives a sensitivity of $\eta = 0.43\ \mu\mathrm{T}/\sqrt{\mathrm{Hz}}$ with the B_{OMW} around 25 μT at $\Delta = -4$ MHz.

IV. BANDWIDTH OF BSE METHOD

A comparison of the BSE and Rabi methods is shown in Fig. 4(a). The sensitivities of the off-resonance method at different frequencies were obtained. Because the sensitivity of the measurement relates to the B_{OMW}, we set a restriction here that the B_{OMW} magnitude is not more than 100 μT. The platform of the sensitivities shown in Fig. 4(a) is about 15 MHz. Those sensitivities are limited by the decay of the signals. Then the sensitivities of the frequencies beyond the platform are limited by the B_{OMW} magnitude which is restricted to 100 μT as mentioned above. The bandwidth of the minimal sensitivity is given by

$$\mathrm{BW} \approx \gamma B_{\mathrm{OWM}}\sqrt{\frac{T_2}{T_2^*}} \tag{8}$$

(details in Appendix G). Compared with the Rabi resonant method [18] in the same condition (details in Appendix F) at an optimized time τ_{MW}, the bandwidth is improved by more than one order of magnitude with an acceptable decrease of the sensitivity.

We then investigated the detecting frequency range of this method. The simulation of the sensitivity calculated from the first period of the BS oscillation with the frequency from DC to 8 GHz is shown in Fig. 4(b). The experiment data shown at several frequencies from 0.8 to 5.5 GHz are in accord with the simulation, which indicates the wideband response frequency range of the off-resonance method. The sensitivities will increase if they are measured with an optimized evolution time τ instead of the first period (details in Appendix H).

The BSE method is an approximation and it fails when the MW is on-resonance. So the method should not work in regions 1 and 2. The results are measured in the $m_s = \{0, -1\}$ subsystem. The Q will be slightly different in the

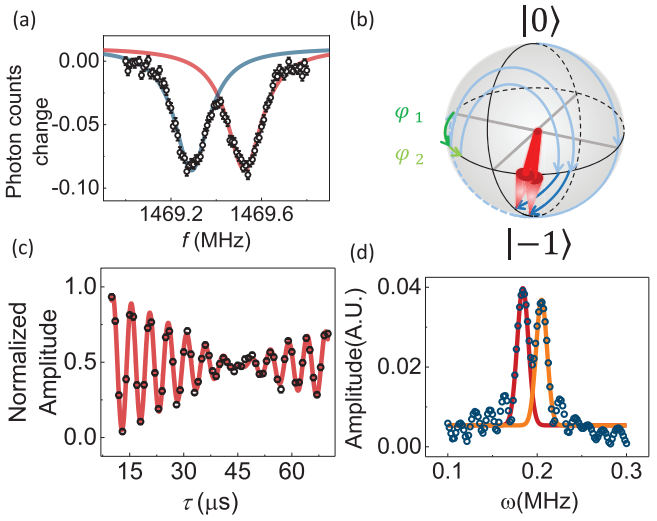

FIG. 5. Frequency measurement. (a) The hyperfine ODMR spectrum from $|0\rangle$ state to $|-1\rangle$ state of ground states of the NV center. The two hyperfine resonance frequencies of the NV center, 1469.29 and 1469.52 MHz, are given by Lorentz fitting separately. (b) The evolution paths in the rotation frame. (c) The BS oscillation (frequency at 0.19 MHz) measured at 1465 MHz is modulated by the beat frequency (4.62 kHz). **(d)** Fast Fourier transformation (blue spots) of the signal in (c).

$ms = \{0, +1\}$ subsystem which is given as:

$$Q_{0,+1} = \frac{2}{f_+ - f} + \frac{1}{f_- + f} + \frac{1}{f_- - f} + \frac{2}{f_+ + f}, \quad (9)$$

but it will give identical results (B_{OMW}) as the $ms = \{0, -1\}$ subsystem prepared.

V. FREQUENCY MEASUREMENT

In the above discussion, we treat the frequency of the MW as known information. In the following, we give access to the frequency measurement while the MW frequency and the amplitude are both unknown. In contrast to the hassles of tuning the static field to search the resonant frequency meticulously, the BSE can be used for extracting the MW frequency from a two-qubit system which consists of an NV center and a nearby ^{13}C nuclear spin. The optically detected magnetic resonance (ODMR) spectrum of the $|0\rangle$ to $|-1\rangle$ state of the NV center splits [Fig. 5(a)] as a result of the hyperfine interaction between the NV center and a nearby ^{13}C nuclear spin [29]. The two closely packed resonant frequencies of the NV center causes it to evolve in two different paths in the Bloch sphere [Fig. 5(b)]. So that the normalized signals oscillate in two different frequencies [Figs. 5(c) and 5(d)] which could be used to resolve the frequency of the under-test MW (details in Appendix I). Finally, the frequency of the MW was recovered as 1464.49 ± 0.95 MHz, which agrees well with the actual input frequency 1465 MHz. Furthermore, instead of using the two-qubit system, measuring the oscillation frequency under several different magnetic fields also enables the extraction of the MW frequency. Hence, by employing an NV center with a nearby nuclear spin or changing the magnetic field for several times, we can routinely achieve the measurements of both the magnitude and the frequency of a MW.

VI. CONCLUSION

In conclusion, we have developed a wideband MW quantum sensing protocol and demonstrated a measurement of the MW magnetic field with frequency ranging from about 0.8 to 5.5 GHz. While the demonstration of the frequency range in this work is limited by the MW circuits, this protocol can also be extended up to terahertz without any requirement of an ultra-high bias magnetic field (details in Appendix J).

With the development of ultrafast electronic technology, this method can be used in the testing and development of the devices. Sometimes, the MW signal may not easily be gated, the BSE method is still working with the free-induction decay (FID) sequence [only two $\pi/2$ pulses without the middle two π pulses shown in Fig. 1(c)]. Though the sensitivities could be worse, we can use a ^{12}C-enriched sample with a dephasing time up to several hundred microseconds [30] to get almost the same sensitivity as this article does. Furthermore, the influence of the diamond to the MW could be ignored (details in Appendix C).

The ability of imaging the MW or magnetic field at nanoscale has already been confirmed by many works [20,31,32]. When the NV center acts as the MW probe, the near-field magnetometry can be achieved. For example, it can be very useful to reveal the MW crosstalk between the transistors of a chip in microcosm.

And the quantum phase estimation algorithm [33] or quantum metrology by quantum entanglement [34] could be used to enhance the sensitivity. Furthermore, given the advantage of the quantum precision measurement and wideband characteristic, this protocol can be developed to be traceable and can potentially be standard in the MW calibrations. It is also worth mentioning that the BSE method could also be used in other quantum systems to measure the MW and give inspiration in the field of magnetometry.

ACKNOWLEDGMENTS

This work was supported by the National Key R&D Program of China (Grants No. 2018YFA0306600, No. 2018YFF01012500, and No. 2016YFA0502400), the NNSFC (Grants No. 81788101, No. 11761131011, No. 11874338, No. 91636217, and No. 11722544), the CAS (Grants No. GJJSTD20170001 and No. QYZDY-SSW-SLH004), Anhui Initiative in Quantum Information Technologies (Grant No. AHY050000), Science and Technological Fund of Anhui Province for Outstanding Youth (1808085J09), and the Fundamental Research Funds for the Central Universities.

R.L. and C.-J.W. contributed equally to this work.

APPENDIX A: BSE FOR AN NV CENTER IN AN OFF-RESONANCE MW FIELD

The Hamiltonian for an NV center is

$$H = H_0 + H_1(t) = DS_z^2 + \gamma B_z S_z + \gamma B_{\mathrm{OMW}} \cos(ft) S_x, \quad (A1)$$

where B_z is the component of the static magnetic field along the NV axis. B_{OMW} and f are the amplitude and frequency

of the off-resonance MW (OMW) magnetic field, respectively. S_x and S_z are the spin-1 Pauli matrices. According to the Schrieffer-Wolff transformation [35], the Hamiltonian could be transformed by a unitary transformation $U(t) = e^{S(t)}$, where $S(t) = -S(t)^\dagger$ to obtain a effective Hamiltonian. $S(t)$ can be written as

$$S(t) = \begin{pmatrix} 0 & S_1(t) & 0 \\ -S_1^*(t) & 0 & S_2(t) \\ 0 & -S_2^*(t) & 0 \end{pmatrix}, \tag{A2}$$

which satisfies $S(t) = -S(t)^\dagger$. $S_1(t)$ and $S_2(t)$ can be written as

$$S_1(t) = -\gamma B_{\mathrm{OMW}} \frac{f_+ e^{-if_+ t} - f_+ \cos(ft) + if\sin(ft)}{\sqrt{2}(f_+ - f)(f_+ + f)},$$
$$S_2(t) = \gamma B_{\mathrm{OMW}} \frac{f_- e^{if_- t} - f_- \cos(ft) - if\sin(ft)}{\sqrt{2}(f_- - f)(f_- + f)}, \tag{A3}$$

where $f_\pm = D \pm \gamma B_z$ are the resonant frequencies of the NV center. The effective Hamiltonian is

$$H_{\mathrm{eff}} \approx H_0 + \frac{1}{2}[S(t), H_1] = H_0 + \gamma B_{\mathrm{OMW}} \cos(ft)\frac{\sqrt{2}}{2} \begin{pmatrix} \frac{S_1(t)+S_1^*(t)}{2} & 0 & \frac{S_1(t)-S_2(t)}{2} \\ 0 & \frac{S_2(t)+S_2^*(t)}{2} - \frac{S_1(t)+S_1^*(t)}{2} & 0 \\ \frac{S_1^*(t)-S_2^*(t)}{2} & 0 & -\frac{S_2(t)+S_2^*(t)}{2} \end{pmatrix}. \tag{A4}$$

The time-dependent part of H_{eff} has no effects on the main conclusion. The time-independent part is

$$H_{\mathrm{eff}}^{'} = H_0 + \begin{pmatrix} A & 0 & \frac{A-B}{2} \\ 0 & B-A & 0 \\ \frac{A-B}{2} & 0 & -B \end{pmatrix}, \tag{A5}$$

$$A = \frac{(\gamma B_{\mathrm{OMW}})^2 f_+}{4(f_+ - f)(f_+ + f)}, \tag{A6}$$

$$B = \frac{-(\gamma B_{\mathrm{OMW}})^2 f_-}{4(f_- - f)(f_- + f)}. \tag{A7}$$

The off-diagonal terms can be omitted because of the presence of the external static field B_z in the case of $B_z \gg B_{\mathrm{OMW}}$. Therefore,

$$H_{\mathrm{eff}}^{'} \approx H_0 + \begin{pmatrix} A & 0 & 0 \\ 0 & B-A & 0 \\ 0 & 0 & -B \end{pmatrix}. \tag{A8}$$

After the pulse sequence shown in Fig. 1(c) of the main text, the population of the $|0\rangle$ state is

$$\begin{aligned} S(\tau) &= |\langle 0|U_x(\pi/2)\exp(-iH_0\tau/2)U_x(\pi)\exp(-iH_{\mathrm{eff}}^{'}\tau)U_x(\pi)\exp(-iH_0\tau/2)U_x(\pi/2)|0\rangle|^2 \\ &= \frac{1}{2}\left\{1 + \cos\left[\frac{(\gamma B_{\mathrm{OMW}})^2\tau}{8}\left(\frac{1}{f_+ - f} + \frac{2}{f_- + f} + \frac{2}{f_- - f} + \frac{1}{f_+ + f}\right)\right]\right\}, \end{aligned} \tag{A9}$$

where $U_x(\pi/2)$ ($U_x(\pi)$) is the coherent manipulation of the $\pi/2$ pulse (π pulse) around the x axis of the NV center. To be convenient, Q and ω are introduced:

$$Q = \frac{1}{f_+ - f} + \frac{2}{f_- + f} + \frac{2}{f_- - f} + \frac{1}{f_+ + f}, \tag{A10}$$

$$\omega = \tfrac{1}{8}(\gamma B_{\mathrm{OMW}})^2 Q. \tag{A11}$$

Obviously, ω is the oscillation frequency of the signal in an experiment and Q can be regarded as a factor involving NV resonant frequency $f_\pm$ and MW frequency f. In the situation where f is close to f_- and $\frac{2}{f_- - f}$ dominate the Q, Eq. (A9) becomes

$$S(\tau) = \frac{1}{2}\left[1 + \cos\left(\frac{(\gamma B_{\mathrm{OMW}})^2\tau}{4(f_- - f)}\right)\right]. \tag{A12}$$

The last $\pi/2$ pulse of the sequence in Fig. 1(c) of the main text could have an arbitrary phase ϕ according to X axis defined by the first $\pi/2$ pulse:

$$U_\phi(\pi/2) = \frac{1}{\sqrt{2}}(1 - i\cos\phi S_x - i\sin\phi S_y). \tag{A13}$$

And the population of the $|0\rangle$ state would be

$$S(\tau) = \tfrac{1}{2}[1 + \cos(\omega\tau + \phi)]. \tag{A14}$$

APPENDIX B: BSE AND AC ZEEMAN EFFECT

The difference between BSE and ac Zeeman effect can be shown by the term of the MW magnetic field vector

decomposition [36]. The Hamiltonian could be written as follows:

$$H = H_0 + H_1 = \left(DS_z^2 + \gamma B_0 S_z\right) + \gamma B_{\mathrm{OMW}} \cos(\omega t) S_x, \tag{B1}$$

$$H_1 = \gamma B_{\mathrm{OMW}} \cos(\omega\tau) S_x = \frac{\gamma B_{\mathrm{OMW}}}{2} S_x (e^{i\omega\tau} + e^{-i\omega\tau}) = \text{“rotating term”} + \text{“counter-rotating term”}. \tag{B2}$$

In the rotating frame with frequency ω, the two terms could be written as

$$\text{Rotating term} = \frac{\gamma B_{\mathrm{OMW}}}{2\sqrt{2}} \begin{pmatrix} 0 & 1 & 0 \\ 1 & 0 & 1 \\ 0 & 1 & 0 \end{pmatrix}, \tag{B3}$$

$$\text{Counter-rotating term} = \frac{\gamma B_{\mathrm{OMW}})}{2\sqrt{2}} \begin{pmatrix} 0 & e^{i2\omega\tau} & 0 \\ e^{-i2\omega\tau} & 0 & e^{i2\omega\tau} \\ 0 & e^{-i2\omega\tau} & 0 \end{pmatrix}. \tag{B4}$$

If we only consider the rotating term with the rotating wave approximation, it is usually called the ac Zeeman effect. The energy shifts due to the counter-rotating term are known as the BSE. And when we obtain the approximation of the counter-rotating term, the rotating term is a default and also included. Though the effect containing both terms is sometimes also called the ac Zeeman effect, here we would like to call it BSE to dissolve the ambiguity and highlight the contribution of the counter-rotating term.

Here we only talk about the linearly polarized MW. If the MW is circularly polarized, the counter-rotating term will not exist, and the MW can also be measured by the ac Zeeman effect with the equation

$$S = \tfrac{1}{2}\cos(\omega\tau), \tag{B5}$$

$$\omega_{0,-1} = \gamma B_{\mathrm{OMW}} \frac{1}{8}\left(\frac{1}{f_+ - f} + \frac{2}{f_- - f}\right), \tag{B6}$$

if we use the $(0, -1)$ subsystem, for example.

APPENDIX C: INFLUENCE OF THE MW DISTRIBUTION OF DIAMOND

The concern about the influence to the original MW field exists in both classical sensors and diamond quantum sensors. Putting a loop antenna or a piece of antenna will change the distribution and magnitude of the MW. However, as the diamond sensor becomes a few microns [37], the influence could be extremely minimized since the size of the tip is far smaller than the wavelength of the MW. Even with the large size diamond, since the permeability of diamond is 1, the influence on the original MW magnetic field is hard to observe [18]. Though the dielectric constant of diamond is very large [38], there is no straightforward relation between the MW magnetic field and electric field in the near field [39]. The existence of the diamond may indeed change the resonant frequency of the cavity; however, the magnetic field distribution could be reconstructed directly by the measurement [38].

APPENDIX D: DECAY DERIVATION

We ignore the influence of the original decoherence of the NV center caused by the ^{13}C bath [40], because the decay rate of the BS oscillation is much faster. The decay of the BS oscillation comes from the natural broadening of the energy level of the ground state of the NV center. The natural broadening could be extracted from the FID signal [40].

$$S_{\mathrm{FID}}(\tau) = \tfrac{1}{2}[1 + \cos(\delta\omega\tau)]\, e^{-(\tau/T_2^*)^2}, \tag{D1}$$

where $\delta\omega$ is the detuning frequency. So the FFT transformation of the S_{FID} gives the line shape of the energy level of the ground state of the NV center.

$$S_{\mathrm{FID}}(f) = \frac{1}{2\pi}\int \frac{1}{2}[1 + \cos(\delta\omega\tau)] e^{-(\tau/T_2^*)^2} e^{-if\tau} d\tau = \frac{1}{2}\left(1 + \frac{1}{\sqrt{2\pi}}\frac{T_2^*}{\sqrt{2}}\frac{e^{-\frac{1}{4}(T_2^*)^2(f-\delta\omega)^2} + e^{-\frac{1}{4}(T_2^*)^2(f+\delta\omega)^2}}{2}\right). \tag{D2}$$

The line shape of S_{FID} is a Gaussian and the standard deviation is $\sigma_f = \frac{\sqrt{2}}{T_2^*}$. According to Eq. (A12) and considering the natural broadening, the BS oscillation could be written as

$$S(\tau) = \int \frac{1}{2}\left[1 + \cos\left(\frac{(\gamma B_{\mathrm{OMW}})^2\tau}{4(f_- - f)}\right)\right] e^{-\frac{f_- - f_{0-}}{2\sigma_f^2}} df_-, \tag{D3}$$

where $f_{0-} = D - \gamma B_z$. Here we denote $\delta = f_{0-} - f$ which is the detuning of the MW frequency and $\Delta f = f_- - f_{0-}$ is the deviation of the energy level of the ground state of the NV center. And we assume that $\delta \gg \Delta f$, so

$$S(\tau) = \frac{1}{\sqrt{2\pi}\sigma_f} \times \int \frac{1}{2}\left[1 + \cos\left(\frac{(\gamma B_{\mathrm{OMW}})^2\tau}{4(f_- - f)}\right)\right] e^{-\frac{f_- - f_{0-}}{2\sigma_f^2}} df_- = \frac{1}{2}\left[1 + \cos\left(\frac{(\gamma B_{\mathrm{OMW}})^2\tau}{4\delta}\right) e^{-\frac{\sigma_f^2(\gamma B_{\mathrm{OMW}})^4\tau^2}{32\delta^4}}\right]. \tag{D4}$$

APPENDIX E: SENSITIVITY OF THE BSE METHOD

The sensitivity of the measurement of an ac field for an NV center can be evaluated by $dB_{\min} = \sigma_S^N / dS_B$ [15], where σ_S^N is the standard deviation after N measurements of the signal S and dS_B is the slope of S variation with B_{OMW}. Here the sensitivity is defined as the minimum distinguishable field in 1 s [41]. Many papers treat the sensitivity and the minimum detectable magnetic field as the same, because their sensitivities are independent of MW magnitude. The minimum detectable magnetic field is the same as the minimum distinguishable field from zero magnetic field. However, in the BSE method, the situation is complicated because the sensitivity depends on the magnitude of the magnetic field. Though the sensitivity of the BSE method describes the ability to distinguish the smallest change in the magnetic field, it cannot distinguish it from zero magnetic field but a certain given magnitude B_{OMW}. So here we only consider the distinguishable ability of the BSE method.

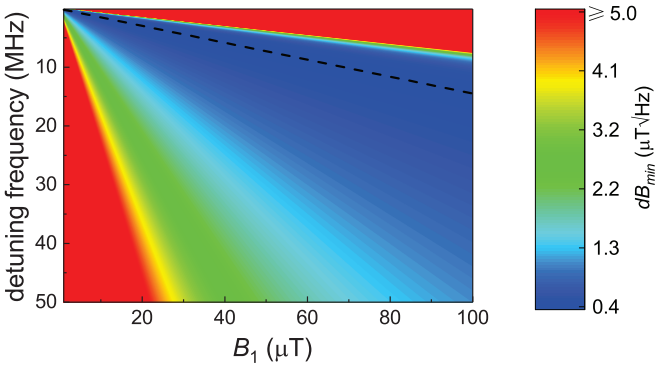

FIG. 6. Simulation of the sensitivity of BSE method. Simulation of sensitivity of different MW frequencies and B_{OMW} magnitudes. Sensitivities larger than 5 $\mu\mathrm{T}/\sqrt{\mathrm{Hz}}$ are set to 5 $\mu\mathrm{T}/\sqrt{\mathrm{Hz}}$. The dashed line in the map indicates the maximum sensitivity.

First we omitted the decay of the oscillation signal, and the dS_B is given as

$$dS_B = \max_{\phi}\left[\left|\frac{1}{8}\gamma^2 B_{\mathrm{OMW}} Q\tau \sin\left(\frac{1}{8}(\gamma B_{\mathrm{OMW}})^2 Q\tau + \phi\right)\right|\right]. \tag{E1}$$

The $\delta B_{\min}$ could be achieved by adjusting ϕ in Eq. (A14), therefore

$$\delta B_{\min} = \frac{8\sigma_S^N}{\gamma^2 Q B_{\mathrm{OMW}}\tau}. \tag{E2}$$

In a single measurement where σ_S is the uncertainty deduced from the shot-noise-limited signal [15], $\sigma_S^N = \sigma_S/\sqrt{N}$, where $N = T/4\tau$. Here τ is the applied time of the off-resonance MW and 4τ is the total time of one experiment. And T is the total experiment time of N measurements.

According to the decay derivation, the maximum sensitivity of the BSE method depends on the B_{OMW} magnitude and the natural broadening of the ground state of the NV center. The simulation of the maximum sensitivities versus different various B_{OMW} magnitudes and frequencies is shown in Fig. 6. In the restriction that B_{OMW} is less than 100 μT here, B_{OMW} continuously changes with the detuning frequency in order to get the maximum sensitivity. In the frequency platform range of 0 ∼ 15 MHz, the maximum sensitivity could be reached with B_{OMW} less than 100 μT. When the frequency is out of the platform range, the maximum sensitivity increases with the detuning frequency because B_{OMW} must equal 100 μT all the time to reach the best sensitivity.

APPENDIX F: SENSITIVITY OF THE RABI METHOD

The Rabi sensitivity is calculated by varying B_{OMW} at a fixed time τ_{mw}. With an off-resonance frequency, the τ_{mw} is optimized by simulating the maximum sensitivity according to the Rabi oscillation equation [18,40,42]

$$P = \left(\frac{(\gamma B_{\mathrm{OMW}})^2}{(\gamma B_{\mathrm{OMW}})^2 + \delta^2}\right)\cos(2\pi\tau\sqrt{(\gamma B_{\mathrm{OMW}})^2 + \delta^2}) \times e^{-(\tau/T_2^*)^2 \frac{\delta^2}{(\gamma B_{\mathrm{OMW}})^2+\delta^2}}. \tag{F1}$$

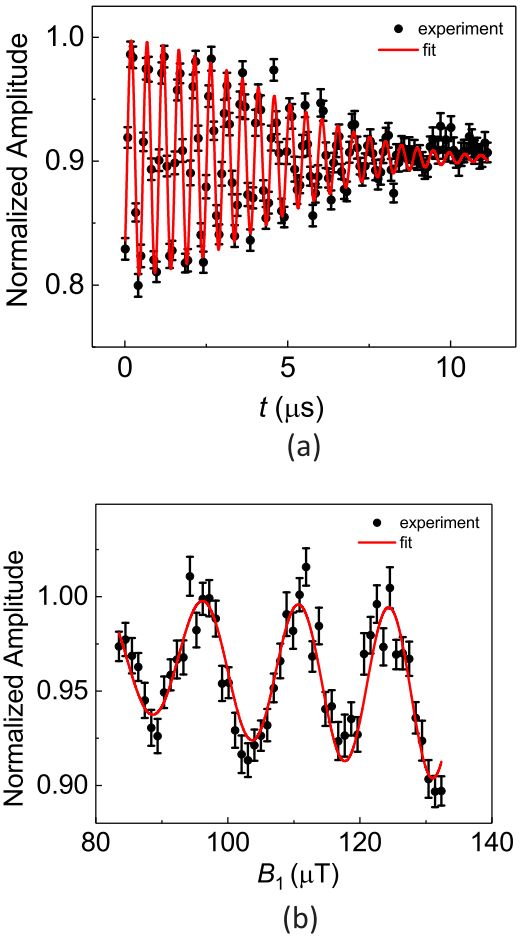

FIG. 7. FID and Rabi decay. (a) FID signal of the NV center measured at a detuning frequency of −2 MHz and $T_2^* = 5.77$ μs. (b) Rabi signal at detuning frequency of −2 MHz.

The T_2^* is fitted from the FID signal [Fig. 7(a)]. The experiment is fitted according to the Eq. (F1) [Fig. 7(b)]. With respect to the resonant frequency, the Rabi oscillation decay becomes much more complicated and faster than the theoretical estimation. The sensitivity could be extracted from the oscillation signal in the same way as in the off-resonance method.

APPENDIX G: BANDWIDTH OF BSE METHOD

The time $\tau = T_2/2$ is chosen to reach the maximum sensitivity. The slope of the signal dS_B is

$$\frac{dS}{dB_{\mathrm{OMW}}} = \frac{1}{2}e^{-\frac{\sigma_f^2(\gamma B_{\mathrm{OMW}})^4\tau^2}{32\delta^4}} \times \sqrt{\left(\frac{\gamma^2\tau B_{\mathrm{OMW}}}{2\delta}\right)^2 + \left(\frac{\sigma_f^2\gamma^4\tau^2 B_{\mathrm{OMW}}^3}{8\delta^4}\right)^2} \times \left[\sin\left(\frac{(\gamma B_{\mathrm{OMW}})^2\tau}{4\delta} + \phi\right)\right]. \tag{G1}$$

The maximum slope $\frac{dS}{dB_{\mathrm{OMW}}}$ corresponds to the maximum sensitivity and phase ϕ could be selected to get the maximum of

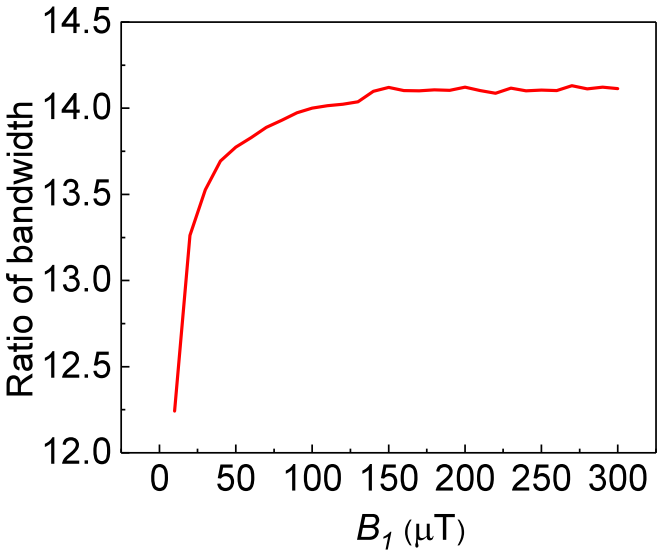

FIG. 8. Ratio of bandwidth. The simulation of the ratio of bandwidth between BSE method and Rabi method. The result shows that BSE method's bandwidth is an order larger than the Rabi method's.

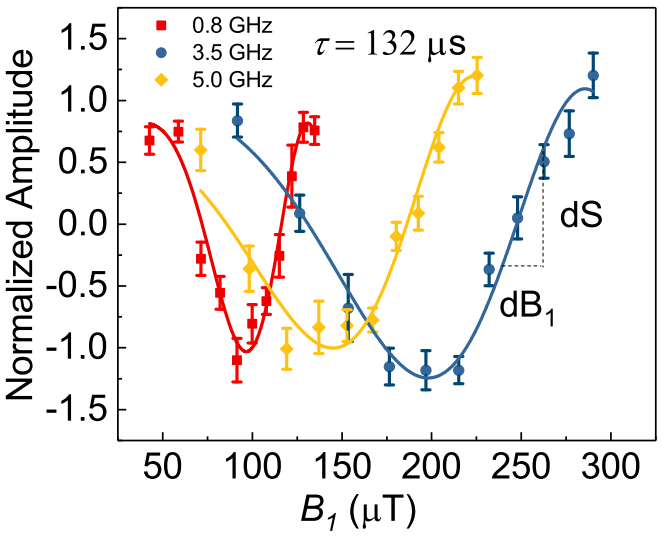

FIG. 9. BS oscillation signal under different MW frequencies. The signals oscillate at different frequencies (0.8, 3.5, and 5 GHz) in the first period with increasing strength of B_{OMW}. The data are fitted by sine curves.

$|\sin(\frac{(\gamma B_{\mathrm{OMW}})^2\tau}{4\delta}+\phi)|$ as described in Appendix A. The second term in the square root is an order smaller than the first term with a large δ as the maximum sensitivity achieved, so it can be neglected:

$$\frac{dS}{dB_{\mathrm{OMW}}} = \frac{1}{2}e^{-\frac{\sigma_f^2(\gamma B_{\mathrm{OMW}})^4\tau^2}{32\delta^4}}\left(\frac{\gamma^2\tau B_{\mathrm{OMW}}}{2\delta}\right). \tag{G2}$$

And the maximum of the slope requires that $\delta = \frac{\gamma B_{\mathrm{OMW}}}{2}\sqrt{\frac{\sigma_f\tau}{2\sqrt{2}}}$. With the $\sigma_f = \sqrt{2}/T_2^*$ and $\tau = \frac{T_2}{2}$, the bandwidth is given as

$$\mathrm{BW} = \gamma B_{\mathrm{OMW}}\sqrt{\frac{T_2}{T_2^*}-\frac{\sqrt{2}}{T_2^*}\frac{1}{1-2\sqrt{\frac{T_2^*}{T_2}}}}. \tag{G3}$$

Here we exclude the range [second term in Eq. (G3)] to ensure that the off-resonance condition is satisfied when the maximum sensitivity is obtained. We then compare the bandwidth of two methods (BSE and Rabi) at different upper limit values of B_{OMW}. As B_{OMW} becomes large enough, the bandwidth of the BSE protocol can be approximated as

$$\mathrm{BW} \approx \gamma B_{\mathrm{OMW}}\sqrt{\frac{T_2}{T_2^*}}. \tag{G4}$$

Figure 8 shows the ratio of the bandwidth (demonstrated in the main text) between BSE and Rabi methods given the different upper limits of the B_{OMW}.

APPENDIX H: WIDE DETECTING FREQUENCY RANGE DEMONSTRATION OF THE BSE METHOD

The off-resonance protocol could be adopted for a wide range of frequencies. Here we set that the sensitivities were measured at the first period of the BS oscillation (Fig. 9). The simulation and the experiment of the sensitivities within the bandwidth from dc to 8 GHz [Fig. 4(b)] are also shown in the main text.

APPENDIX I: FREQUENCY MEASUREMENT DERIVATION

The frequency of the under tested MW could be extracted by the magnetometry. The NV center coupled by a ^{13}C causes BS oscillation with two frequencies:

$$\omega_1 = (\gamma B_{\mathrm{OMW}})^2\frac{1}{4(f-f_-)},$$
$$\omega_2 = (\gamma B_{\mathrm{OMW}})^2\frac{1}{4(f-f'_-)}. \tag{I1}$$

The f_- and f'_- are the two resonance frequencies of the NV center split by the coupling of the ^{13}C. So the frequency of the under tested MW f is

$$f = f_- + (f_- - f'_-)\frac{\omega_2}{\omega_1-\omega_2}. \tag{I2}$$

The detectable range of the frequency could be extracted according to the decay theory of the BS oscillation. According to Eq. (D4),

$$S(\tau) = \frac{1}{2}\left[1+\frac{1}{2}\left(\cos(\omega_1\tau)e^{-\frac{\sigma_f^2\omega_1^2\tau^2}{2\delta^2}}+\cos(\omega_2\tau)e^{-\frac{\sigma_f^2\omega_2^2\tau^2}{2\delta'^2}}\right)\right]. \tag{I3}$$

The linewidths of the frequencies of the ω_1 and ω_2 of the FFT of the $S(\tau)$ are $\frac{\sigma_f\omega_1}{\delta}$ and $\frac{\sigma_f\omega_2}{\delta'}$, respectively. In order to detect the frequency of the off-resonance MW according to Eq. (I2), the linewidth should be smaller than the difference of the two BS oscillation frequencies $|\omega_1-\omega_2|$. So that

$$|\omega_1-\omega_2| > \frac{1}{2}\left(\frac{\sigma_f\omega_1}{\delta}+\frac{\sigma_f\omega_2}{\delta'}\right). \tag{I4}$$

With the approximation $\delta, \delta' \gg \sigma_f$ and Eq. (I2), Eq. (I4) requires that

$$|f_- - f'_-| > \sigma_f, \tag{I5}$$

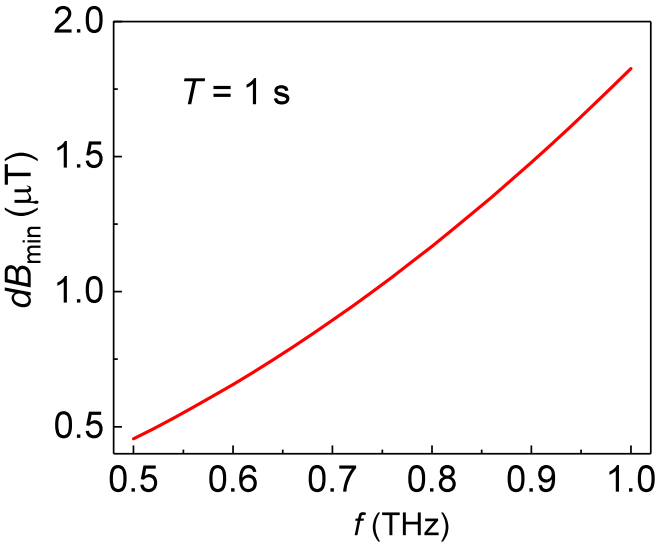

FIG. 10. Sensitivity of THz band. The simulation sensitivities in THz range with the quantum-projection-noise limitation.

which means that the coupling of the ^{13}C should be resolved first, which is obvious.

Except for the limitation of the linewidth of the FFT signal mentioned above, the original decoherence of the NV center caused by the ^{13}C nucleus spin bath that we ignored before also affects the detectable range of the frequency measurement. The resolution of the linewidth discussed above is also limited by the decoherence time T_2:

$$|\omega_1 - \omega_2| > \frac{1}{T_2}, \tag{I6}$$

which leads the detectable range of the frequency of the under tested microwave to be

$$|f - f_-| < \frac{\gamma B_{\mathrm{OMW}}}{2}\sqrt{(f_- - f'_-)T_2}. \tag{I7}$$

APPENDIX J: TERAHERTZ BAND SIMULATION

We simulated the performance of the BSE method in the THz range (Fig. 10) by assuming $B_{\mathrm{OMW}} = 10$ mT [43] and $B_z = 1$ T to estimate the sensitivities in the quantum-projection-noise limitation [15] with $T_2 = 0.6$ s (the decoherence time of the NV center) which we measured. Here we assume the single-shot readout [44] could be used to remove the photon noise and the technical noise could be ignored with fine craftsmanship. The result theoretically shows the ability of the THz range magnetometry of the BSE method.

[1] S.-Y. Wu, C. Lin, M. Chiang, J. Liaw, J. Cheng, S. Yang, C. Tsai, P. Chen, T. Miyashita, C. Chang *et al.*, in *Electron Devices Meeting (IEDM), 2016 IEEE International* (IEEE, New York, 2016) pp. 2-6.

[2] J. Briaire and S. Krisch, IEEE Trans. Comput.-Aided Des. Integr. Circuits Syst. **19**, 645 (2000).

[3] T. Dubois, S. Jarrix, A. Penarier, P. Nouvel, D. Gasquet, L. Chusseau, and B. Azaïs, IEEE Trans. Instrum. Meas. **57**, 2398 (2008).

[4] R. J. Fontana, IEEE Trans. Microwave Theory Tech. **52**, 2087 (2004).

[5] C. A. Balanis, Proc. IEEE **80**, 7 (1992).

[6] M. Kanda, IEEE Trans. Compat Electromagn **36**, 261 (1994).

[7] N. N. Mai-Khanh, T. Iizuka, A. Sasaki, M. Yamada, O. Morita, and K. Asada, IEEE Trans. Instrum. Meas. **64**, 840 (2015).

[8] B. H. Calhoun, Y. Cao, X. Li, K. Mai, L. T. Pileggi, R. A. Rutenbar, and K. L. Shepard, Proc. IEEE **96**, 343 (2008).

[9] J. A. Gordon, C. L. Holloway, S. Jefferts, and T. Heavner, in *Electromagnetic Compatibility (EMC), 2010 IEEE International Symposium on* (IEEE, New York, 2010) pp. 321–324.

[10] C. L. Holloway, J. A. Gordon, S. Jefferts, A. Schwarzkopf, D. A. Anderson, S. A. Miller, N. Thaicharoen, and G. Raithel, IEEE Trans. Antennas Propag. **62**, 6169 (2014).

[11] M. Wahnschaffe, H. Hahn, G. Zarantonello, T. Dubielzig, S. Grondkowski, A. Bautista-Salvador, M. Kohnen, and C. Ospelkaus, Appl. Phys. Lett. **110**, 034103 (2017).

[12] P. Böhi, M. F. Riedel, T. W. Hänsch, and P. Treutlein, Appl. Phys. Lett. **97**, 051101 (2010).

[13] C. F. Ockeloen, R. Schmied, M. F. Riedel, and P. Treutlein, Phys. Rev. Lett. **111**, 143001 (2013).

[14] R. Black, F. Wellstood, E. Dantsker, A. Miklich, D. Koelle, F. Ludwig, and J. Clarke, Appl. Phys. Lett. **66**, 1267 (1995).

[15] J. Maze, P. Stanwix, J. Hodges, S. Hong, J. Taylor, P. Cappellaro, L. Jiang, M. G. Dutt, E. Togan, A. Zibrov *et al.*, Nature **455**, 644 (2008).

[16] G. Balasubramanian, I. Chan, R. Kolesov, M. Al-Hmoud, J. Tisler, C. Shin, C. Kim, A. Wojcik, P. R. Hemmer, A. Krueger *et al.*, Nature **455**, 648 (2008).

[17] F. Shi, F. Kong, P. Zhao, X. Zhang, M. Chen, S. Chen, Q. Zhang, M. Wang, X. Ye, Z. Wang *et al.*, Nat. Methods **15**, 697 (2018).

[18] P. Wang, Z. Yuan, P. Huang, X. Rong, M. Wang, X. Xu, C. Duan, C. Ju, F. Shi, and J. Du, Nat. Commun. **6**, 6631 (2015).

[19] I. Jakobi, P. Neumann, Y. Wang, D. B. R. Dasari, F. El Hallak, M. A. Bashir, M. Markham, A. Edmonds, D. Twitchen, and J. Wrachtrup, Nat. Nanotech. **12**, 67 (2017).

[20] P. Appel, M. Ganzhorn, E. Neu, and P. Maletinsky, New J. Phys. **17**, 112001 (2015).

[21] M. Dong, Z. Hu, Y. Liu, B. Yang, Y. Wang, and G. Du, Appl. Phys. Lett. **113**, 131105 (2018).

[22] T. Joas, A. M. Waeber, G. Braunbeck, and F. Reinhard, Nat. Commun. **8**, 964 (2017).

[23] Y. Niu, Y. Li, D. Jin, L. Su, and A. V. Vasilakos, Wireless Networks **21**, 2657 (2015).

[24] C. Wei, A. S. Windsor, and N. B. Manson, J. Phys. B: At. Mol. Opt. Phys. **30**, 4877 (1997).

[25] L. I. Sacolick, F. Wiesinger, I. Hancu, and M. W. Vogel, Magn. Reson. Med. **63**, 1315 (2010).

[26] J. Zhang, A. M. Souza, F. D. Brandao, and D. Suter, Phys. Rev. Lett. **112**, 050502 (2014).

[27] V. Jacques, P. Neumann, J. Beck, M. Markham, D. Twitchen, J. Meijer, F. Kaiser, G. Balasubramanian, F. Jelezko, and J. Wrachtrup, Phys. Rev. Lett. **102**, 057403 (2009).

[28] M. Steiner, P. Neumann, J. Beck, F. Jelezko, and J. Wrachtrup, Phys. Rev. B **81**, 035205 (2010).

[29] R. Epstein, F. Mendoza, Y. Kato, and D. Awschalom, Nat. Phys. **1**, 94 (2005).
[30] P. C. Maurer, G. Kucsko, C. Latta, L. Jiang, N. Y. Yao, S. D. Bennett, F. Pastawski, D. Hunger, N. Chisholm, M. Markham *et al.*, Science **336**, 1283 (2012).
[31] D. R. Glenn, K. Lee, H. Park, R. Weissleder, A. Yacoby, M. D. Lukin, H. Lee, R. L. Walsworth, and C. B. Connolly, Nat. Methods **12**, 736 (2015).
[32] M. S. Grinolds, S. Hong, P. Maletinsky, L. Luan, M. D. Lukin, R. L. Walsworth, and A. Yacoby, Nat. Phys. **9**, 215 (2013).
[33] G. Waldherr, J. Beck, P. Neumann, R. Said, M. Nitsche, M. Markham, D. Twitchen, J. Twamley, F. Jelezko, and J. Wrachtrup, Nat. Nanotech. **7**, 105 (2012).
[34] V. Giovannetti, S. Lloyd, and L. Maccone, Science **306**, 1330 (2004).
[35] H. Wang and G. Burkard, Phys. Rev. B **90**, 035415 (2014).
[36] D. Budker, D. F. Kimball, D. Kimball, and D. P. DeMille, *Atomic Physics: An Exploration Through Problems and Solutions* (Oxford University, Oxford, 2004).
[37] P. Maletinsky, S. Hong, M. S. Grinolds, B. Hausmann, M. D. Lukin, R. L. Walsworth, M. Loncar, and A. Yacoby, Nat. Nanotech. **7**, 320 (2012).
[38] K. Bayat, J. Choy, M. Farrokh Baroughi, S. Meesala, and M. Loncar, Nano Lett. **14**, 1208 (2014).
[39] J. A. Sedlacek, A. Schwettmann, H. Kübler, and J. P. Shaffer, Phys. Rev. Lett. **111**, 063001 (2013).
[40] R. Hanson, V. Dobrovitski, A. Feiguin, O. Gywat, and D. Awschalom, Science **320**, 352 (2008).
[41] A. Grosz, M. J. Haji-Sheikh, and S. C. Mukhopadhyay, *High Sensitivity Magnetometers* (Springer, Berlin, 2017) p. 567.
[42] V. V. Dobrovitski, A. E. Feiguin, R. Hanson, and D. D. Awschalom, Phys. Rev. Lett. **102**, 237601 (2009).
[43] B. Knyazev, G. Kulipanov, and N. Vinokurov, Meas. Sci. Technol. **21**, 054017 (2010).
[44] P. Neumann, J. Beck, M. Steiner, F. Rempp, H. Fedder, P. R. Hemmer, J. Wrachtrup, and F. Jelezko, Science **329**, 542 (2010).